11C.6

FETCH- AND DURATION-LIMITED NATURE OF SURFACE WAVE GROWTH INSIDE TROPICAL CYCLONES AND MICROWAVE REMOTE SENSING OF HURRICANE WIND SPEED USING DOMINANT WAVE PARAMETERS

Paul A. Hwang[1], Xiaofeng Li[2], Biao Zhang[3,4], and Edward J. Walsh[5]
[1]Remote Sensing Division, Naval Research Laboratory, Washington, DC, USA
[2]GST, NOAA/NESDIS, College Park, MD, USA
[3]School of Marine Sciences, Nanjing University of Information Science and Technology, Nanjing, Jiangsu, China
[4]Jiangsu Research Center for Ocean Survey and Technology, Nanjing, Jiangsu, China
[5]Physical Sciences Division, NOAA/ Earth System Research Laboratory, Boulder, Colorado

1. INTRODUCTION

Airborne and satellite “remote sensing of surface winds” is a misnomer. What’s really measured by various microwave “wind” sensors are ocean surface waves. This is why satellite sensors produce global ocean synoptic surface vector winds but not land surface winds although humans are land dwellers and it would be useful to provide the detailed wind fields over the land habitat.

The microwave wind (wave) sensing techniques can be roughly divided into three broad categories according to the length scales of waves sensed by the instrument: (a) short scale (Bragg resonance roughness), (b) intermediate scale (tilting facets), and (c) long scale (energetic dominant waves). Category (a) includes active scatterometer, synthetic aperture radar (SAR) and passive radiometer. Category (b) includes radar altimeter and Global Navigation Satellite Systems reflectometry (GNSS-R). Category (c) includes radar altimeter, SAR, and potentially GNSS-R.

Scatterometer and radiometer are the primary spaceborne instruments providing the global ocean surface vector wind measurements. At the present, the spatial resolution is about 12.5 km. For highly variable wind fields such as those in coastal areas, mountain gap winds and hurricanes, SAR is frequently employed for its high spatial resolution, which reaches sub-km scale and represents a powerful means for resolving delicate features such as the hurricane eye structure (e.g., Li et al. 2012) and sharp horizontal gradient in the wind field (e.g., Monaldo 2000).

One limiting factor of the SAR or scatterometer wind sensing is the signal saturation in high winds. Several detailed airborne measurements of Ku- and C-band (13.5 and 5.3 GHz) ocean surface backscattering in hurricane hunter flights provide ample evidence of decreased sensitivity toward high winds, as well as saturation and dampening of co-polarized (VV and HH for vertical transmit vertical receive and horizontal transmit horizontal receive) normalized radar cross section (NRCS) over a wide range of incidence angle, azimuth angle and wind speed (e.g., Donnelly et al. 1999; Fernandez et al. 2006).

Early analyses of RADARSAT-2 C-band full-polarization measurements reveal two unusual properties of the cross-polarized backscattering (VH or HV for vertical transmit horizontal receive or vice versa): (a) the wind speed sensitivity increases toward higher wind speeds, and (b) no evidence of wind speed saturation in the available datasets – up to about 26 m/s (Hwang et al. 2010; Vachon and Wolff 2011; Zhang et al. 2011). As more cross-polarization data are reported (e.g., van Zadelhoff et al. 2014; Zhang et al. 2014), VH signal saturation at wind speeds as low as 32 m/s is noticed (Hwang et al. 2014, 2015). Meissner et al. (2014) report the analysis result of L-band VV, HH and VH NRCS from the Aquarius satellite. The highest wind speed is the data set is close to 35 m/s. The signal saturation problem is also evident for all polarizations.

This paper addresses two important aspects of the signal saturation issue: (a) its underlying cause from the point of view of surface wave properties, and (b) how to overcome the signal saturation problem. In section 2, we investigate the first subject and examine several published reports on microwave radar backscattering from the ocean surface in high winds. The connection between the NRCS and ocean surface roughness is discussed in section 3. The properties of the short and intermediate scale waves are mainly determined by the ocean surface wind stress, which is connected to the surface wind speed by a drag coefficient. Recent measurements have shown a nonmonotonic behavior of the ocean surface drag coefficient as a function of wind speed. The main cause of the NRCS saturation may be attributed to the nonmonotonic surface drag coefficient in high winds (section 4).

In contrast to the short and intermediate scale ocean surface roughness, for which the wind stress is the main driving mechanism, the dominant wave parameters (significant wave height and spectral peak wave period) depend on wind speed monotonically. This is because the nonlinear wave-wave interaction plays an important role in the dynamics of the energetic wave components near the spectral peak that contribute the lion’s share to the dominant wave parameters (Section 5).

In section 6, we present a hurricane wind retrieval algorithm using dominant wave parameters. The full set of the wind-wave triplets (U_{10}, H_s, T_p) can be calculated with the fetch- or duration-limited growth function knowing only one of three variables and accompanied with the fetch or duration information (Hwang 2016). The wind retrieval algorithm is developed from the fetch-limited wave growth functions based on about one quarter of the total dataset of wind and wave measurements collected inside Hurricane Bonnie 1998 (Wright et al. 2001; Hwang 2016). Application of the algorithm to the full dataset serves as verification. The fetch-law wind retrieval algorithm is then applied to two SAR images of two hurricanes. Compared to the wind retrieved with the geophysical model function (GMF), the result shows good agreement in the azimuthal segment within about 30° of the radar pointing direction. Section 7 is a summary.

2. SATURATION OF MICROWAVE BACKSCATTERING

As discussed in the Introduction, many field measurements of airborne NRCS have shown signal saturation in high winds (e.g., Donnelly et al. 1999;

Fernandez et al. 2006). Fig. 1 plots the Ku- and C-band VV and HH NRCS (σ_0) in hurricane conditions reported by Fernandez et al. (2006). These are digitized from their Figs. 5 to 8, showing the NRCS at 4 similar incidence angles each (between 29 and 50°) for the two frequency bands and two polarizations. For the Ku band, the nonmonotonic wind speed dependency for both polarizations is quite prominent over a wide range of incidence angles. The nonmonotonic trend for the C band is somewhat milder than the Ku band but the loss of wind sensitivity toward high winds is obvious.

Meissner et al. (2014) report L band (1.4 GHz) VV, HH, and VH NRCS data from the Aquarius satellite with wind speed coverage from 0 to 35 m/s and 3 incidence angles (29.4°, 38.4° and 46.3°). The results are plotted in Fig. 1c. The wind speed saturation behavior is very similar for the three polarization states.

SAR has been used as a high spatial resolution scatterometer for studying hurricanes and mountain gap winds in coastal regions (e.g., Chunchuzov et al. 2000; Monaldo 2000; Monaldo et al. 2001, 2015; Li et al. 2004; Hwang et al. 2010, 2014, 2015; Zhang et al. 2011, 2012, 2014; Horstmann et al. 2013, 2015; van Zadelhoff et al. 2014). Fig. 2 shows several examples of spaceborne RADARSAT-2 dual-polarization (VV and VH) NRCS measurements plotted against reference wind speed U10 (Hwang et al. 2015). The wind sources are ocean wind wave buoys, stepped frequency microwave radiometer (SFMR) and H*Wind product for the left column (Zhang et al. 2014), exclusively SFMR measurements in several hurricane hunter missions for the middle column (van Zadelhoff et al. 2014), and European Center for Mid-range Weather Forecast (ECMWF) numerical model output for the right column (van Zadelhoff et al. 2014). The top row shows VV and the bottom row shows VH. The trend of signal saturation is detectable in both VV and VH. The possible exception of the VH saturation in the ECMWF dataset (Fig. 2f) may be caused by the much coarser spatial resolution of the numerical model (the SAR resolution is degraded to match the numerical model resolution for this dataset). In general, the critical wind speed (incidence angle dependent) at which NRCS starts to saturate is lower in VV than in VH. Also, the range of incidence angles with signal saturation problem is broader in VV than in VH.

3. SURFACE ROUGHNESS DEPENDENCE ON WIND STRESS

Understanding the NRCS dependence on short scale waves is one of the main motivations of studying short scale waves by oceanographers. Here we examine the causes of NRCS signal saturation through the connection of the NRCS and the surface roughness, which is contributed by the ocean surface waves for radar backscattering from the ocean surface. For the vertical polarization (VV), Bragg resonance is the dominant contributor of backscattering in moderate incidence angles. The VV NRCS σ_{0VV} can be expressed symbolically as (e.g., Valenzuela 1978):

$$\sigma_{0VV}\left(f,\theta,U_{10}\right)=G_{VV}\left(f,\theta,U_{10}\right)B\left(k_B,U_{10}\right), \quad (1)$$

where G_{VV} is the scattering coefficient, B is the dimensionless surface roughness spectrum, and k is wavenumber and subscript B indicates the Bragg resonance surface roughness component. The 1D dimensionless spectrum $B(k)$ is related to the 1D surface waves spectrum $S(k)$ by $B(k)=k^3S(k)$. The modification of the relative permittivity from air entrained by wave breaking impacts the Fresnel reflection coefficient so the scattering coefficient is a function of f, θ and U_{10}. The net impact of the entrained air is to decrease reflection and increase transmission; thus the effects of increasing roughness and air entrainment from increasing wind are additive in enhancing passive microwave emission but counter each other for active microwave scattering. The detail is discussed by Hwang (2012) and Hwang and Fois (2015).

Here we focus on the ocean surface roughness. A brief review of field measurements of short waves and more extensive discussions of the connection between NRCS and surface roughness is given by Hwang et al. (2013). The efforts of ocean surface roughness measurements in the ocean have led to the discovery of a similarity relationship expressing the dimensionless roughness spectral component $B(k)$ as a function of dimensionless wind forcing factor given by the ratio u_*/c, where u_* is wind friction velocity and c is the phase speed of the surface roughness spectral component (Hwang and Wang 2004a):

$$B\left(\frac{u_*}{c};k\right)=A(k)\left(\frac{u_*}{c}\right)^{a(k)}. \quad (2)$$

The proportionality constant A and exponent a of the power-law function vary with the wavenumber. Fig. 3 shows examples of scatter plots illustrating the similarity relationship for several wave components with k ranging from 2.1 to 300 rad/m for the wind-sea and mixed-sea data groups. The least squared fitting curve for each group is shown with a line segment of the same color as the data. Also shown in the figure is the equilibrium spectrum (e.g., Phillips 1985; Hwang et al. 2000): $B_e\left(u_*/c;k\right)=5.2\times10^{-2}\left(u_*/c\right)$ with a dashed-dotted line for each spectral component. Increasing deviation from the equilibrium spectral function toward the shorter wave component is clearly shown.

Because k and c are connected by the dispersion relationship: $c^2=g/k+\tau k$, the roughness spectral similarity relationship is used as a parameterization function of the H roughness spectrum model (Hwang 2005; Hwang et al. 2013), i.e., $B\left(u_*/c;k\right)=B\left(k;U_{10}\right)$. The spectral parameterization function is initially built on in-situ measurements of $A(k)$ and $a(k)$ using fast-response wave gauges mounted on a free-drifting and wave-following instrument platform. These results were obtained from several years field campaigns conducted in the Gulf of Mexico (Hwang and Wang 2004a). Figs. 4a and 4b plot the $A(k)$ and $a(k)$ derived from the wind-sea and mixed-sea field data groups with solid and dashed curves, respectively.

For the vertical polarization radar backscattering, Bragg resonance plays a critical role (1), thus microwave radar can be treated as a spectrometer of the ocean surface roughness. Using the Ku-, C- and L-band GMFs, Hwang et al. (2013) retrieve the Bragg resonance surface roughness spectral components of the three microwave frequency bands (Fig. 4c). Expressed in the similarity function form (2), for low to moderate wind conditions (u_*/c <~3) the results of microwave spectrometer analysis (shown with diamonds, circles and squares for Ku, C and L bands in Figs. 4a and 4b) are in good agreement with in-situ free-drifting wave gauge (FDWG) data. For higher wind conditions (u_*/c >~3), the wind speed exponent (*a*) becomes almost identical for all wave components (Fig. 4c).

The GMFs are derived from global radar data with wind speed coverage ranging from calm to hurricane wind conditions. Their analysis results compensate for the limited coverage of the in-situ data in both geographical locations and environmental conditions. Combining in-situ FDWG data and GMF radar spectrometer analysis, Hwang and Fois (2015) show that NRCS computations using the H spectrum are in agreement with Ku-, C-, and L-band VV GMFs to within about +3 and -2 dB for wind speeds less than 60 m/s and incidence angles between 20 and 50°.

The results outlined in this subsection represent a critical link between microwave scattering and the ocean surface roughness. The link is particularly useful for examining the wind speed dependency of both NRCS and ocean surface roughness.

4. SURFACE ROUGHNESS SATURATION

Figure 5a shows the 1D roughness spectra for wind speeds from 5 to 60 m/s in 5 m/s steps and $\omega_\#$= U_{10}/c_p=$\omega_p U_{10}/g$ =2.5, where *c* and ω=2π/*T* are the phase speed and angular frequency of a wave component, subscript *p* indicates the spectral peak component, *T* is wave period and *g* is gravitational acceleration. The dimensionless spectrum $B(k)=k^3S(k)$ is presented here since the cubic *k* weighting emphasizes the short and intermediate scale components (large *k*). The relatively young wave age (c_p/U_{10}=1/$\omega_\#$=0.4) is selected for the representative conditions observed inside the broad region of the hurricane coverage except near the eye region (Hwang 2016) based on analyzing the 60 wave spectra collected by airborne scanning radar altimeter (SRA) reported by Wright et al. (2001), further discussion of the analysis of hurricane waves is given in section 6.

Figure 5b plots the wind speed dependency of the Bragg resonance spectral components $B(k_B)$ at Ku, C and L bands calculated for the 45° incidence angle. There are two notable regions where the short waves show apparent non-monotonic dependence on U_{10}: (i) between U_{10} = 15 and 20 m/s in the neighborhood of the Ku-band Bragg resonant wave components (around *k* = 400 rad/m), and (ii) for U_{10}>50 m/s over a broad wavenumber range. The former [(i)] is caused by the change of wind speed exponent *a* of the similarity function (2) in the region u_*/c >~3 as illustrated in Fig. 4c. This is an artifact resulted from approximating the gradual variation of the exponent in the neighborhood of u_*/c =3 by two linear segments employed by Hwang et al. (2013). A more sophisticated representation of the u_*/c transition in Fig. 4c for the roughness spectrum parameterization should be able to remove this artifact.

The latter [(ii)] is a consequence of the non-monotonic behavior of the ocean surface wind drag coefficient and surface wind stress (proportional to the square of the wind friction velocity u_*) as a function of wind speed (Fig. 6). An extensive discussion of the drag coefficient and its effect on NRCS computation has been presented by Hwang et al. (2013). In Fig. 6, additional drag coefficient data collected inside hurricanes (Powell 2006; Holthuijsen et al. 2012) are added (labelled P06 and H12, respectively). Of special interest are the two groups of P06 data collected inside and outside the 30-km circle from the hurricane center. The drag coefficients for the inside group are considerably lower than those of the outside group. This likely reflects the swell effect reducing the surface wind stress (e.g., Pan et al. 2005; Hwang et al. 2011a; García-Nava et al. 2012; Potter 2015). In a recent analysis of the 2D wavenumber spectra collected by airborne SRA in hurricane hunter missions reported by Wright et al. (2001), the characteristic wave ages are distinctly different inside and outside the 30-km circle from the hurricane center. The wave conditions inside the circle are clearly contaminated by swell (mixed seas) and those outside the circle are relatively young wind seas (Hwang 2016).

The hurricane data labelled H12 in Fig. 6 include those based on the average of a large number (1452) of wind profiles as well as subgroups sorted into left, right and rear (back) sectors with respect to the hurricane heading. The solid line is the fitted curve using the data marked "Open ocean" as discussed in Hwang (2011) and Hwang et al. (2013)

$$C_{10} = 10^{-5}\left(-0.16U_{10}^2 + 9.67U_{10} + 80.58\right). \qquad (3)$$

This drag coefficient formula captures the feature of saturation and dampening of the wind stress in high winds and is used in the H spectrum computation shown in Fig. 5. According to these drag coefficient observations, the wind stresses, or correspondingly wind friction velocities, above and below 50 m/s may have the same value and therefore produce similar ocean surface roughness. For example, as shown in Fig. 5a the roughness spectrum in the short and intermediate length scales at 60 m/s (category 4 hurricane wind speed) is the same as that at 38 m/s (category 1 hurricane). This may result in serious underprediction of the hurricane intensity from SAR imagery.

The tilting slopes of intermediate scale waves represent the critical surface roughness property important to microwave altimeter and GNSS-R remote sensing applications. An example of the tilting slopes integrating to k_u =9.54 rad/m (corresponding to the tilting scale of GNSS-R L-band frequency) is shown in Fig. 5c for mature ($\omega_\#$=0.83) and young ($\omega_\#$=2.50) seas. Saturation of tilting slopes is also expected as a consequence of the non-monotonic wind stress dependence on wind speed.

It is emphasized here that the saturation of short and intermediate scale waves occurs in other wave spectral models using wind stress (with a non-monotonic dependence on wind speed) as the driving force (e.g., Phillips 1985; Donelan and Pierson 1987; Elfouhaily et al. 1997), e.g., see the NRCS computations using the E (Elfouhaily et al. 1997) and the H spectra presented in Hwang and Fois (2015).

5. DOMINANT WAVE PROPERTIES AND WIND WAVE GROWTH FUNCTIONS

Although short and intermediate scale waves contribute significantly to the ocean surface roughness, their role in the dominant wave properties such as the significant wave height is negligible because the surface displacement spectrum decreases as a power-law function of wavenumber. For the azimuthally integrated 1D spectrum $S(k)$, the exponent of the power law is about -2.5, thus the spectral density levels at wavenumbers 2, 4, 8 and 16 times of the spectral peak wavenumber are 0.18, 0.031, 0.0055 and 0.00098 times of the spectral peak value. The contribution to the significant wave height thus decreases rapidly toward high wavenumber.

The most important factor in the similarity relationship of the surface wave spectrum in the energetic region near the spectral peak is $\omega_\#=U_{10}/c_p$ (e.g., Hasselmann et al. 1973; Donelan et al. 1985; Komen et al. 1994; Young 1999; Janssen 2004). Consequently, for the same wave growth condition, i.e., same $\omega_\#$, the spectral peak downshifts monotonically with wind speed; the spectral similarity thus leads to the monotonic relationship between U_{10} and the dominant wave properties H_s and T_p.

Figure 7a shows the same set of wave spectra as those of Fig. 5a (U_{10}=5, 10, 15, … 60 m/s, and $\omega_\#=U_{10}/c_p=2.5$) but the displacement spectra $S(k)$ are presented to highlight the monotonic downshifting of the energetic portion of the spectrum. For any other inverse wave age $\omega_\#$, the downshift of the spectral peak follows the dispersion relationship $k_p = g/c_p^2 = g\omega_\#^{-2}U_{10}^{-2}$, therefore also with a monotonic dependency between k_p and U_{10}.

The significant wave height integrated from the wave spectrum (labelled H15) is shown in Fig. 7b for $\omega_\#$=0.83 and 2.5, illustrating the monotonic increase with wind speed; the result based on the Pierson and Moskowitz (1964) fully developed spectral model (labelled PM) is also shown for comparison with the mature case. Note that for very high wind speeds (usually in hurricanes with limited fetch and finite duration over a region), the conditions for wind-wave full development rarely occur, the theoretical ~80 m wave height at 60 m/s is unlikely to happen (fortunately).

6. OBTAINING HURRICANE WIND SPEED FROM DOMINANT WAVE PARAMETERS

An extensive literature exists showing that the surface waves generated by hurricane winds can be described by the fetch-limited wave growth functions established with data collected under steady wind forcing conditions, e.g., see detailed analyses of buoy recordings within 8 times the hurricane maximum wind radius described in Young (1998, 2006) and Hu and Chen (2011). The robust wave growth similarity relation is also applicable to the wave fields produced by unsteady wind fields such as the rapidly increasing or decreasing mountain gap winds (e.g., García-Nava et al. 2009; Romero and Melville 2010; Ocampo-Torres et al. 2011; Hwang et al. 2011b). In a recent study, Hwang (2016) uses the data of wind-wave triplets obtained by an SRA inside Hurricane Bonnie 1998 (Wright et al. 2001) to derive an empirical formula for the effective wind fetch and effective wind duration in the three major sectors of a hurricane: right, left and back (Black et al. 2007). Fig. 8 summarizes the wind-wave similarity relations expresses as (a) fetch-limited growth, (b) duration-limited growth, and (c) a wave age similarity function. For reference, the dashed and solid curves are the first- and second-order polynomial curves fitting through the reference dataset: BHDDB, which is an assembly of five field experiments under quasi-steady wind forcing and neutral stability conditions discussed in Hwang and Wang (2004). In the wave age range of hurricane waves that can be classified as wind seas (inverse wave age $\omega_\#$ less than about 0.8), the data can be fitted by the first- and second-order curves equally well; the first-order equations are much simpler to work with:

$$\begin{aligned}
&\eta_\# = 6.19\times10^{-7}x_\#^{0.81};\ \omega_\# = 11.86x_\#^{-0.24}\\
&\eta_\# = 1.27\times10^{-8}t_\#^{1.06};\ \ \omega_\# = 36.92t_\#^{-0.31}\ .\\
&\eta_\# = 2.94\times10^{-3}\omega_\#^{-3.42}
\end{aligned} \tag{4}$$

The dimensionless fetch and duration are given by $x_\# = x_f g/U_{10}^2$, $t_\# = t_d g/U_{10}$, and the dimensionless variance is $\eta_\# = \eta_{rms}^2 g^2/U_{10}^4$, where $\eta_{rms} = H_s/4$.

The full set of the wind-wave triplets (U_{10}, H_s, T_p) can be calculated with the fetch- or duration-limited growth function knowing only one of three variables and accompanied with the fetch or duration information. For example, expressing the fetch-limited equations in dimensional variables:

$$\begin{aligned}
&\frac{\eta_{rms}^2 g^2}{U_{10}^4} = 6.19\times10^{-7}\left(\frac{x_f g}{U_{10}^2}\right)^{0.81}\\
&\frac{\omega_p U_{10}}{g} = 11.86\left(\frac{x_f g}{U_{10}^2}\right)^{-0.24}
\end{aligned}\ , \tag{5}$$

which provides two equations for the four unknowns ($\eta_{rms} = H_s/4$, $\omega_p=2\pi/T_p$, U_{10} and x_f; g=9.8 m/s^2 is a constant), so the wind-wave triplets can be solved with any one of the three variables together with fetch x_f. Similarly, the duration-limited functions can be written out in the same fashion, and the wind-wave triplets can be solved with any one of the three variables together with duration t_d. For example, from the fetch-limited growth function, the wind speed can be calculated with the H_s and $x_{\eta x}$ input by solving the first equality in (2)

$$U_{10}\left(H_s, x\right) = 397.46H_s^{0.841}x_f^{-0.341}\ . \tag{6}$$

The application of the concept to the SRA dataset shows very encouraging results (Hwang 2016). The agreement between the fetch- or duration-function derived wave parameters from wind speed or wind speed from wave parameters are in very good agreement with the reference SRA wave measurements and HRD wind speed, except for the region near the hurricane eye. The regression statistics (based on the data outside the 30 km circle) of the bias, slope of linear fitting curve, root mean squares (rms) difference and correlation coefficient, respectively B, s, D and R^2, are listed in table 1. The correlation coefficient is greater than 0.88 for H_s and T_p from U_{10}; 0.85 for U_{10} from H_s and T_p using the fetch function, and 0.60 and 0.65 using the duration function. The quality of U_{10} retrieval using H_s is considerably better than that of using T_p (correlation coefficient of 0.85 vs. 0.60 to 0.64; rms difference of 2.8 to 3.1 m/s vs. 4.5 to 5.2 m/s), see Table 1 of Hwang (2016), which is reproduced here for convenience.

Making use of these results, here we make an attempt to retrieve hurricane wind speed using the SAR-derived dominant wave properties. Hwang (2016) calculated the fetch $x_{\eta x}$ and duration $t_{\omega x}$ for the cyclonic hurricane wind field (analogous to a race track) by solving (5) with the 60 SRA wind-wave triplets reported in Wright et al. (2001). The fetch is fitted with a linear function of the distance from the hurricane center r (both length parameters are in km in the next equation) for each of in three hurricane sectors: right, left and back respectively for the azimuth angles 0-135°, 135-225° and 225-360° referenced to the hurricane heading [the angle increases counterclockwise (CCW)]

$$x_{\eta x} = \begin{cases} -0.26r + 259.79, & right \\ 1.25r + 58.25, & left \\ 0.71r + 30.02, & back \end{cases} . \qquad (7)$$

Subscript ηx in (7) indicates that the fetch is derived from fetch-limited growth function governing the wave variance, and correspondingly the significant wave height [the first equality of (2)]. This algorithm is established with the published 60 SRA spectra collected in Bonnie 1998 on 24-25 August (Wright et al. 2001). The full set of measurements during the mission contains 233 spectra. Here, we apply the algorithm to the full dataset for verification. The results are shown in Fig. 9. Panel (a) shows the scatter plot of $U_{10}\left(H_s, x_{\eta x}\right)$ vs. the Hurricane Research Division (HRD) reference: U_{10}(HRD). The statistics of [B (m/s), s, D (m/s), R^2] for those measurements with $r \geq 45$ km are [-1.51, 0.96, 3.59, 0.82]. The ratio $R_U = U_{10}\left(H_s, x_{\eta x}\right)/U_{10}\left(HRD\right)$ is shown in panels (b), (c) and (d) as functions of r, ϕ and $\omega_{\#}$, respectively. Except in the region near the hurricane eye, the ratio mostly stays within 10 % of the reference, that is, R_U is mostly within 1±0.1, and there is no indication of signal saturation problem in high winds as that encountered in scatterometer wind retrieval; the maximum wind speed in the dataset is 46 m/s. The region with poor results occurs for r<45 km, whereas the radius of hurricane coverage is about 250 km; so U_{10} derived using the fetch growth function is in good agreement with the HRD U_{10} over more than 95% of the hurricane coverage area. These results demonstrate the usefulness of the algorithm of hurricane wind retrieval using the dominant wave parameters.

For application to the spaceborne SAR measurements, two RADARSAT (C-band) images (one each for Bonnie at 23:20:11 UTC 25 Aug 1998 and Ivan at 09:06:19 UTC 06 Sep 2004) are used for the case study. The SAR-derived H_s uses the algorithm of Monaldo and Lyzenga (1986), which has been implemented at NOAA/NESDIS for operational application. For comparison with the fetch function retrieved U_{10}, the reference wind speed is based on the CMOD5 GMF applied to the RADARSAT NRCS.

Figure 10 presents the result of wind retrieval using the fetch growth function. Limiting the data to within ± 30° of the radar look direction and the distance between 50 and 300 km from the hurricane center, the statistics of [B (m/s), s, D (m/s), R^2] are [1.13, 1.06, 2.99, 0.53] for the Bonnie image (Fig. 9a), and [1.01, 1.05, 2.50, 0.69] for the Ivan image (Fig. 9b).

7. SUMMARY

Field measurements and radar spectrometer analysis of ocean surface roughness indicate that the growth of short and intermediate scale roughness spectral components is controlled by the surface wind stress, which is proportional to the wind friction velocity squared and relates to wind speed squared by a drag coefficient. Recent wind profile measurements inside hurricanes show that the drag coefficient dependence on wind speed is nonmonotonic (Fig. 6). Consequently, u_* reaches a maximum at U_{10} about 50 m/s and then decreases as U_{10} increases further. As a result, the high wind ocean surface roughness conditions above and below 50 m/s may not be distinguishable. For example, based on the C_{10} formula established on the dropsonde data inside hurricanes as shown in Fig. 6, the surface roughness spectrum (Fig. 5a) in the short and intermediate length scales important to microwave remote sensing at 60 m/s (category 4 hurricane) is essentially the same as that at about 38 m/s (category 1 hurricane). Wind retrieval methods relying on the microwave signatures reflecting the short and intermediate scale roughness properties, such as scatterometers and altimeters, may have difficulty separating the two wind speed conditions.

To avoid the ambiguity, we seek methods of hurricane wind retrieval using the dominant wave information (significant wave height and spectral peak wave period). Because nonlinear wave-wave interaction plays an important role in the evolution near the energetic spectral peak region, the continuous downshift of the spectral peak component in increasing wind results in a monotonic relationship between wind speed and significant wave height or dominant wave period.

Making use of the wind wave analyses showing that the wave fields inside hurricanes are primarily wind seas except in a small area near the hurricane center (Hwang 2016), an algorithm is developed for hurricane wind speed retrieval using the dominant wave information. The database for the algorithm development is the 60 SRA wave spectra collected in category 2 hurricane Bonnie 1998 (Wright et al. 2001). The full set of the wind-wave triplets (U_{10}, H_s, T_p) can be calculated with the fetch- or duration-limited growth function knowing only one of three variables and accompanied with the fetch or duration information. The results are used to develop a wind retrieval algorithm to obtain hurricane wind speed using the SAR-derived H_s. Applying the algorithm to two SAR images of hurricanes, the fetch-law and GMF derived wind speeds are in good agreement in an azimuthal sector (about 30° wide) in the radar look direction.

References

Black, P. G., E. A. D'Asaro, W. M. Drennan, J. R. French, P. P. Niiler, T. B. Sanford, E. J. Terrill, E. J. Walsh, and J. A. Zhang, 2007: Air-sea exchange in hurricanes: Synthesis of observations from the coupled boundary layer air-sea transfer experiment. *Bulle. Am. Meteorol. Soc.*, **88**, 357-374.

Chunchuzov, I., P. W. Vachon, and X. Li, 2000: Analysis and modeling of atmospheric gravity waves observed in RADARSAT SAR images. *Remote Sensing Env.*, **74**, 343-361,

Donelan, M. A., and W. J. Pierson, 1987: Radar scattering and equilibrium ranges in wind-generated waves with application to scatterometry. *J. Geophys. Res.*, **92**, 4971-5029.

Donelan, M. A., J. Hamilton, and W. H. Hui, 1985: Directional spectra of wind-generated waves, *Phil. Trans. Roy. Soc. Lond.*, **A315**, 509-562

Donnelly, W. J., J. R. Carswell, R. E. McIntosh, P. S. Chang,

J. Wilkerson, F. Marks, and P. G. Black, 1999: Revised ocean backscatter models at C and Ku band under high-wind conditions. *J. Geophys. Res.,* **104**, 11485-11497.

Elfouhaily, T., B. Chapron, K. Katsaros, and D. Vandemark, 1997: A unified directional spectrum for long and short wind-driven waves. *J. Geophys. Res.,* **102***,* 15781-15796.

Fernandez, D. E., J. R. Carswell, S. Frasier, P. S. Chang, P. G. Black, and F. D. Marks, 2006: Dual-polarized C- and Ku-band ocean backscatter response to hurricane-force winds. *J. Geophys. Res.*, **111**, C08013, doi:10.1029/2005JC003048.

García-Nava, H., F. J. Ocampo-Torres, P. Osuna, and M. A. Donelan, 2009: Wind stress in the presence of swell under moderate to strong wind conditions. *J. Geophys. Res.*, **114**, C12008, doi:10.1029/2009JC005389.

García-Nava, H., F. J. Ocampo-Torres, P. A. Hwang, and P. Osuna, 2012: Reduction of wind stress due to swell at high wind conditions. *J. Geophys. Res*., 117, C00J11, doi:10.1029/2011JC007833.

Hasselmann, K. et al., 1973: Measurements of wind-wave growth and swell decay during the Joint North Sea Wave Project (JONSWAP). *Deutsch. Hydrogr. Z.*, Suppl. **A8(12)**, 95pp.

Holthuijsen, L. H., M. D. Powell, and J. D. Pietrzak, 2012: Wind and waves in extreme hurricanes. *J. Geophys. Res.,* **117**, C09003.

Hu, K., and Q. Chen, 2011: Directional spectra of hurricane-generated waves in the Gulf of Mexico. *Geophys. Res. Lett.*, **38**, L19608, doi:10.1029/2011GL049145.

Hwang, P. A., 2006: Duration- and fetch-limited growth functions of wind-generated waves parameterized with three different scaling wind velocities. *J. Geophys. Res*., **111**, C02005, doi:10.1029/2005JC003180.

Hwang, P. A., 2011: A note on the ocean surface roughness spectrum. *J. Atmos. Ocean. Tech*., **28**, 436-443, doi: 10.1175/2010JTECHO812.1.

Hwang, P. A., 2012: Foam and roughness effects on passive microwave remote sensing of the ocean. *IEEE Trans. Geos. Rem. Sens.,* **50**, 2978-2985.

Hwang, P. A., 2016: Fetch- and duration-limited nature of surface wave growth inside tropical cyclones: With applications to air-sea exchange and remote sensing. *J. Phys. Oceanogr*., **46**, 41-56, doi: 10.1175/JPO-D-15-0173.1.

Hwang, P. A., and F. Fois, 2015: Surface roughness and breaking wave properties retrieved from polarimetric microwave radar backscattering. *J. Geophys. Res*., **120**, 3640-3657, doi:10.1029/2015JC010782.

Hwang, P. A., and D. W. Wang, 2004a: An empirical investigation of source term balance of small scale surface waves. *Geophys. Res. Lett*., **31**, L15301, doi:10.1029/2004GL020080.

Hwang, P. A., and D. W. Wang, 2004b: Field measurements of duration limited growth of wind-generated ocean surface waves at young stage of development. *J. Phys. Oceanogr.*, **34**, 2316-2326. (Corrigendum, **35**, 268-270, 2005).

Hwang, P. A., D. W. Wang, E. J. Walsh, W. B. Krabill, and R. N. Swift, 2000: Airborne measurements of the directional wavenumber spectra of ocean surface waves. Part 1. Spectral slope and dimensionless spectral coefficient. *J. Phys. Oceanogr.*, **30**, 2753-2767.

Hwang, P. A., B. Zhang, J. V. Toporkov, and W. Perrie, 2010: Comparison of composite Bragg theory and quad-polarization radar backscatter from RADARSAT-2: With applications to wave breaking and high wind retrieval. *J. Geophys. Res*., **115**, C08019, doi:10.1029/2009JC005995.

Hwang, P. A., H. García-Nava, and F. J. Ocampo-Torres, 2011a: Dimensionally consistent similarity relation of ocean surface friction coefficient in mixed seas. *J. Phys. Oceanogr*., **41**, 1227-1238, doi: 10.1175/2011JPO4566.1.

Hwang, P. A., H. García-Nava, and F. J. Ocampo-Torres, 2011b: Observations of wind wave development in mixed seas and unsteady wind forcing. *J. Phys. Oceanogr*., **41**, 2343-2362, doi: 10.1175/JPO-D-11-044.1.

Hwang, P. A., D. M. Burrage, D. W. Wang, and J. C. Wesson, 2013: Ocean surface roughness spectrum in high wind condition for microwave backscatter and emission computations. *J. Atmos. Oceanic Tech.*, **30**, 2168-2188, doi: 10.1175/JTECH-D-12-00239.1.

Hwang, P. A., W. Perrie, and B. Zhang, 2014: Cross polarization radar backscattering from the ocean surface and its dependence on wind velocity. *IEEE Geos. Rem. Sens. Lett*., **11**, 2188-2192, doi: 10.1109/LGRS.2014.2324276.

Hwang, P. A., A. Stoffelen, G.-J. van Zadelhoff, W. Perrie, B. Zhang, H. Li, and H. Shen, 2015: Cross polarization geophysical model function for C-band radar backscattering from the ocean surface and wind speed retrieval. *J. Geophys. Res*., **120**, 893-909, doi:10.1029/2014JC010439.

Janssen, P., 2004: *The Interaction of Ocean Waves and Wind*. Cambridge Univ. Press, Cambridge, UK, 300 pp.

Komen, G. J., L. Cavaleri, M. Donelan, K. Hasselmann, S. Hasselmann, and P. A. E. M. Janssen (Eds.), 1994: *Dynamics and modeling of ocean waves.* Cambridge Univ. Press, Cambridge, UK, 532 pp.

Li, X., C. Dong, P. Clemente-Colon, W. G. Pichel, and K. S. Friedman, 2004: Synthetic aperture radar observation of the sea surface imprints of upstream atmospheric solitons generated by flow impeded by an island. *J. Geophys. Res.*, **109**, C02016, doi:10.1029/2003JC002168.

Li, X., J. A. Zhang, X. Yang, W. G. Pichel, M. DeMaria, D. Long, and Z. L, 2012: Tropical cyclone morphology from spaceborne synthetic aperture radar. *Bulle. Am. Meteor. Soc.*, **94**, 215-230, doi:10.1175/BAMS-D-11-00211.1.

Meissner, T., F. J. Wentz, and L. Ricciardulli, 2014: The emission and scattering of L-band microwave radiation from rough ocean surfaces and wind speed measurements from the Aquarius sensor. *J. Geophys. Res.*, **119**, 6499-6522.

Monaldo, F. M., 2000: The Alaska SAR demonstration and near-real-time synthetic aperture radar winds. *JHU APL Tech. Digest*, **21**, 75-79.

Monaldo, F. M., and D. R. Lyzenga, 1986: On the estimation of slope- and height-variance spectra from SAR imagery. *IEEE Trans. Geos. Remote Sensing*, **24**, 543-550.

Monaldo, F. M., D. T. Thompson, R. C. Beal, W. G. Pichel, and P. Clemente-Colón, 2001: Comparison of SAR-derived wind speed with model predictions and ocean buoy measurements. *IEEE Trans. Geos. Remote Sensing*, **39**, 2587-2600.

Monaldo, F. M., C. R. Jackson, W. G. Pichel, and X. Li (2015), A weather eye on coastal winds, *Eos, 96*, doi :10.1029/2015EO034581.

Ocampo-Torres, F. J., H. García-Nava, R. Durazo, P. Osuna, G. M. Díaz Méndez, and H. C. Graber, 2011: The INTOA Experiment: A study of ocean-atmosphere interactions under moderate to strong offshore winds and opposing swell conditions, in the Gulf of Tehuantepec, Mexico. *Bound.-Layer Meteorol*., doi: 10.1007/s10546-010-9561-5, **138**, 433-451.

Pan, J., D. W. Wang, and P. A. Hwang, 2005: A study of wave effects on wind stress over the ocean in a fetch-limited case. *J. Geophys. Res.*, **110**, C02020, doi:10.1029/2003JC002258.

Phillips, O. M., 1985: Spectral and statistical properties of the equilibrium range in wind-generated gravity waves. *J. Fluid Mech.*, **156**, 505-531.

Pierson, W. J., and L. Moskowitz, 1964: A proposed spectral form for full, developed wind seas based on the similarity theory of S.A. Kitaigorodskii. *J. Geophys. Res.*, **69**, 5181-5190.

Potter, H., 2015: Swell and the drag coefficient. *Ocean Dyn.*, **65**, 375-384.

Powell, M. D., 2006: Drag coefficient distribution and wind speed dependence in tropical cyclones. Final Report to the NOAA JHT Program, 26 pp.

Romero, L., and W. K. Melville, 2010: Airborne observations of fetch-limited waves in the Gulf of Tehuantepec. *J. Phys. Oceanogr.*, **40,** 441-465.

Valenzuela, G. R., 1978: Theories for the interaction of electromagnetic and oceanic waves – A review. *Bound.-Layer Meteorol.,* **13**, 61-85.

van Zadelhoff, G.-J., A. Stoffelen, P. W. Vachon, J. Wolfe, J. Horstmann, and M. Belmonte Rivas, 2014: Retrieving hurricane wind speeds using cross polarization C-band measurements. *Atmos. Meas. Tech.,* **7**, 437-449.

Wright, C. W., E. J. Walsh, D. Vandemark, W. B. Krabill, A. W. Garcia, S. H. Houston, M. D. Powell, P. G. Black, and F. D. Marks, 2001: Hurricane directional wave spectrum spatial variation in the open ocean. *J. Phys. Oceanogr.*, **31**, 2472-2488.

Young, I. R., 1988: Parametric hurricane wave prediction model, *ASCE J. Waterway, Port, Coastal and Ocean Eng.,* **114**, 637-652.

Young, I. R., 1998: Observations of the spectra of hurricane generated waves. *Ocean Eng.,* **25**, 261-276.

Young, I. R., 1999: *Wind generated ocean waves.* Elsevier, Amsterdam, the Netherlands, 288 pp.

Young, I. R., 2006: Directional spectra of hurricane wind waves. *J. Geophys. Res.,* **111**, C08020.

Zhang, B., W. Perrie, and Y. He, 2011: Wind speed retrieval from RADARSAT-2 quad-polarization images using a new polarization ratio model. *J. Geophys. Res.,* **116**, C08008.

Zhang, B., and W. Perrie, 2012: Cross-polarized synthetic aperture radar: a new potential technique for hurricanes. *Bull. Amer. Meteor. Soc.,* **93**, 531-541, doi:10.1175/BAMS-D-11-00001.1.

Zhang, B., W. Perrie, P. Vachon, J. A. Zhang, E. W. Uhlhorn, and Y. He, 2014: High resolution hurricane vector winds from C-band dual-polarization SAR observations. *J. Atmos. Oceanic Tech.*, **31**, 272-286.

Table 1. Regression statistics (bias, slope of linear fitting curve, rms difference and correlation coefficient, B, s, D and R^2, respectively) of wind and wave parameters retrieved from one of the three variables in the triplets (U_{10}, H_s, T_p), combining with the empirical design fetch and duration formula (6) and the wind wave growth functions (2). Reproduced from Hwang (2016).

	B (m/s)	s	D (m/s)	R^2
$T_p(U_{10}, x_{\omega x})$	-0.11	0.99	0.75	0.90
$H_s(U_{10}, x_{\eta x})$	-0.03	1.00	0.74	0.92
$T_p(U_{10}, t_{\omega t})$	-0.14	0.99	0.85	0.88
$H_s(U_{10}, x_{\eta t})$	-0.07	1.00	0.83	0.91
$U_{10}(T_p, x_{\omega x})$	0.98	1.03	5.24	0.60
$U_{10}(H_s, x_{\eta x})$	0.27	1.01	3.07	0.85
$U_{10}(T_p, x_{\omega t})$	0.88	1.02	4.49	0.64
$U_{10}(H_s, x_{\eta t})$	0.42	1.01	2.83	0.85

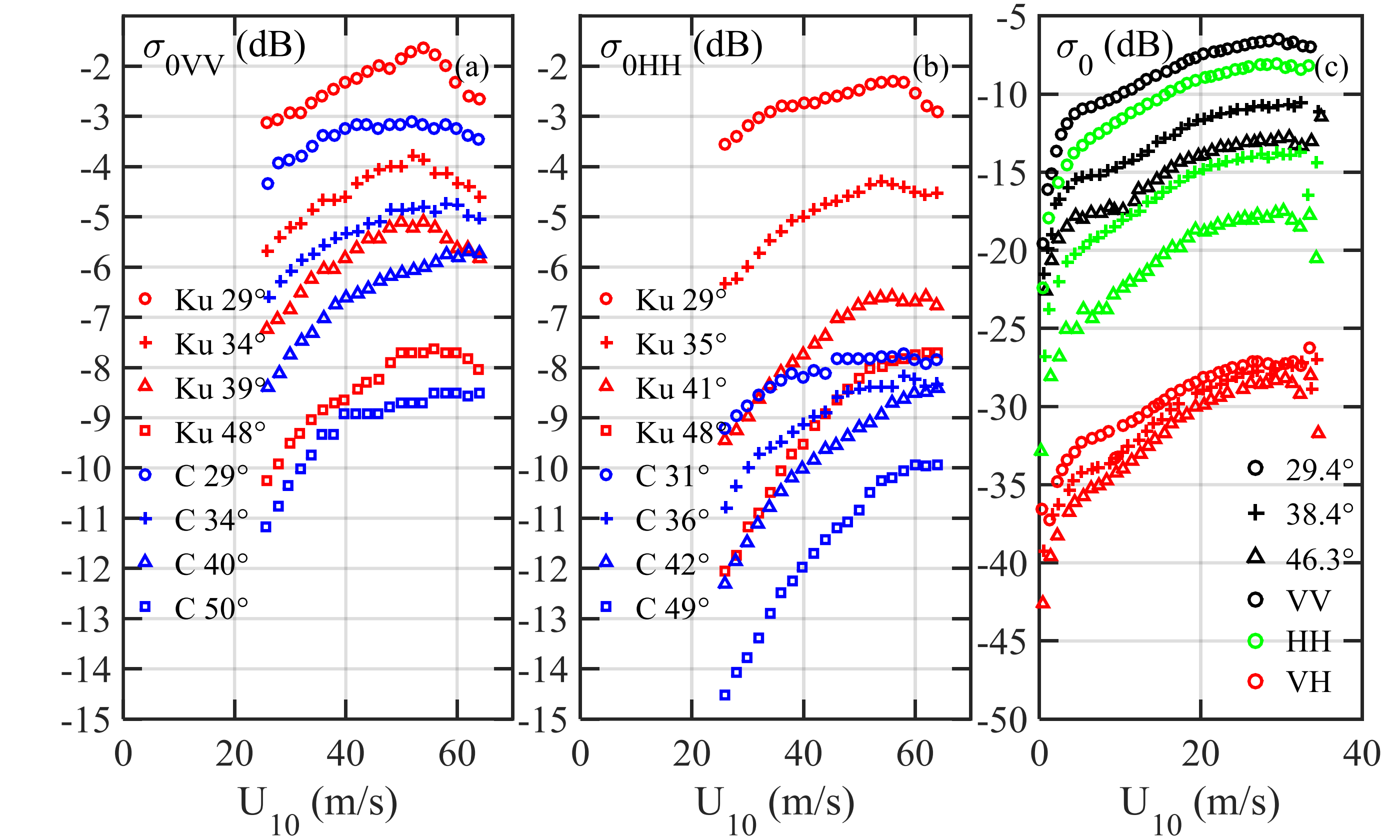

Fig. 1. (a) VV, and (b) HH polarization Ku- and C-band radar backscattering dependence on wind speed from airborne measurements in hurricanes, and (c) L-band VV, HH and VH radar backscattering dependence on wind speed from spaceborne measurements; (a) and (b) are digitized from Figures 5 to 8 of Fernandez et al. (2006), (c) is digitized from Figure 1 of Meissner et al. (2014).

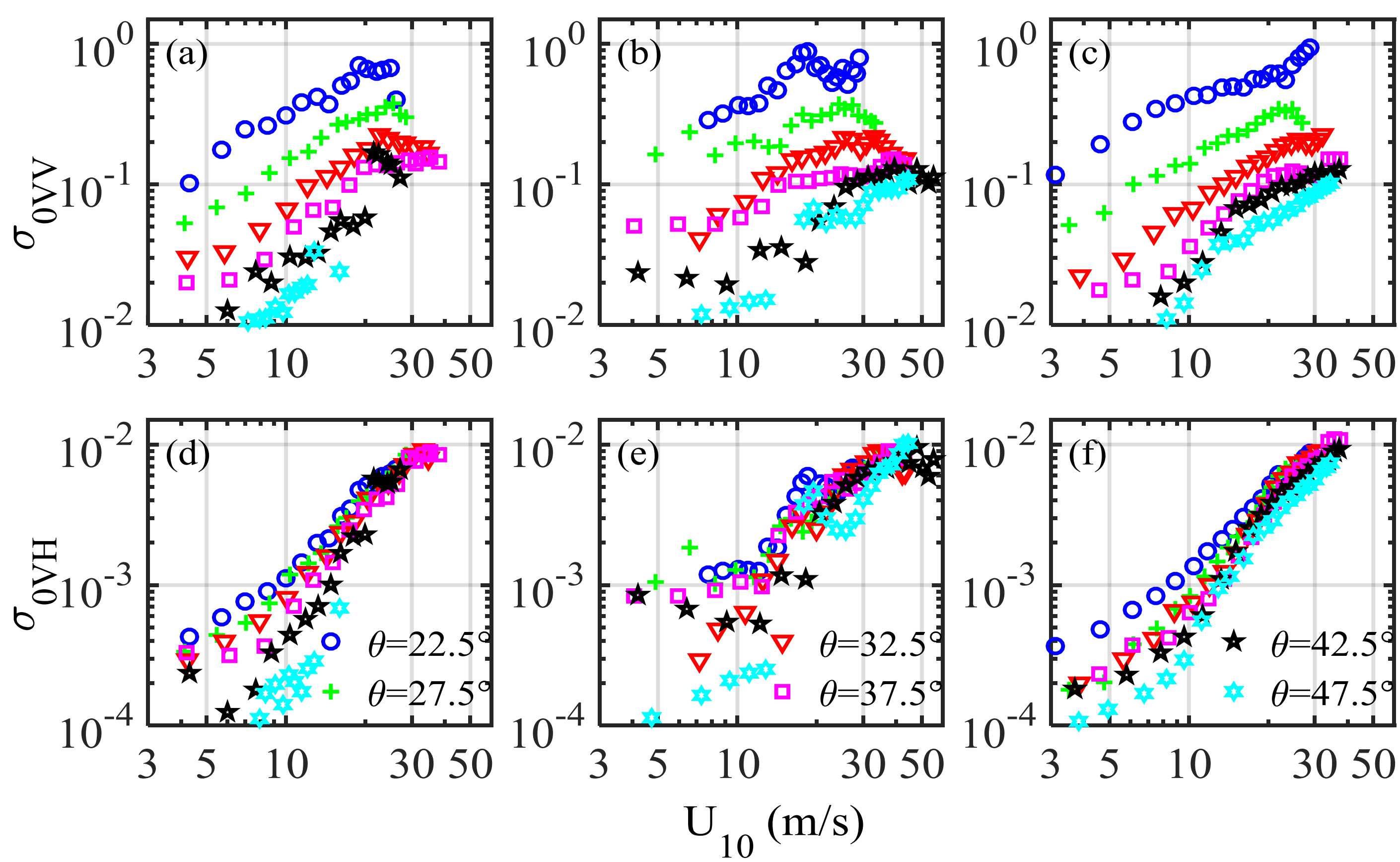

Fig. 2. RADARSAT-2 C-band radar backscattering dependence on wind speed: (top row: a, b, c) VV polarization, (bottom row: d, e, f) VH polarization; sources of wind speeds in the left column (a and d) are combined buoy, SFRM and H*Wind dataset; SFRM for the middle column (b and e); and ECMWF numerical output in the right column (c and f). Further description of these data is given in Hwang et al. (2015).

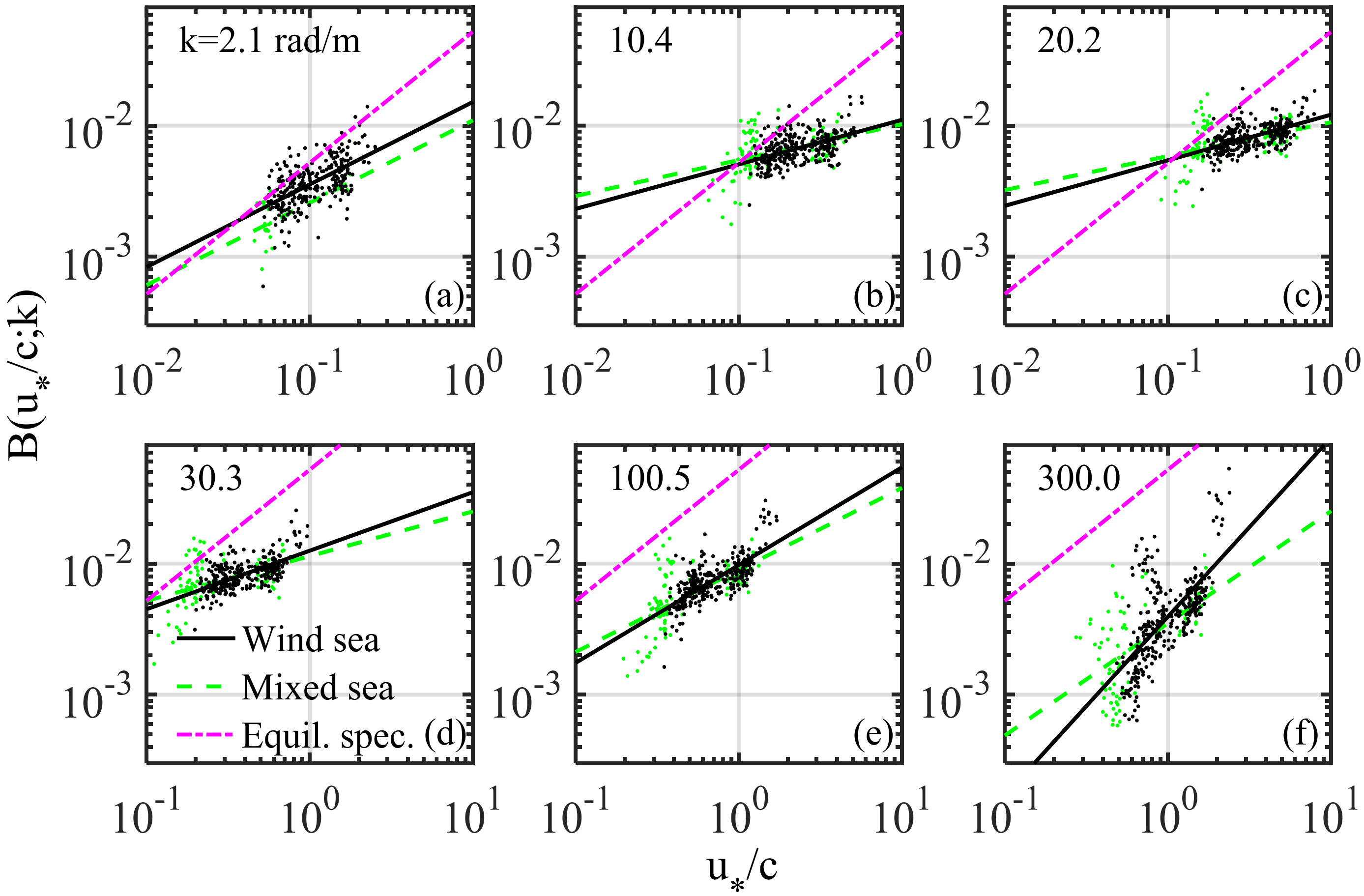

Fig. 3. Similarity relationship of short and intermediate scale ocean surface wave spectral components: (a) k=2.1 rad/m, (b) k=10.4 rad/m, (c) k=20.2 rad/m, (d) k=30.3 rad/m, (e) k=100.5 rad/m, and (f) k=300.0 rad/m. Dark-colored dots are wind seas and light-colored dots are mixed seas; the Fig. 3. Similarity relationship of short and intermediate scale ocean surface wave spectral components: (a) k=2.1 rad/m, (b) k=10.4 rad/m, (c) k=20.2 rad/m, (d) k=30.3 rad/m, (e) k=100.5 rad/m, and (f) k=300.0 rad/m. Dark-colored dots are wind seas and light-colored dots are mixed seas; the corresponding fitted curves are shown with line segments of the same colors. The dashed-dotted line segment (magenta) is the equilibrium spectrum. Further description of these data is given in Hwang and Wang (2004a).

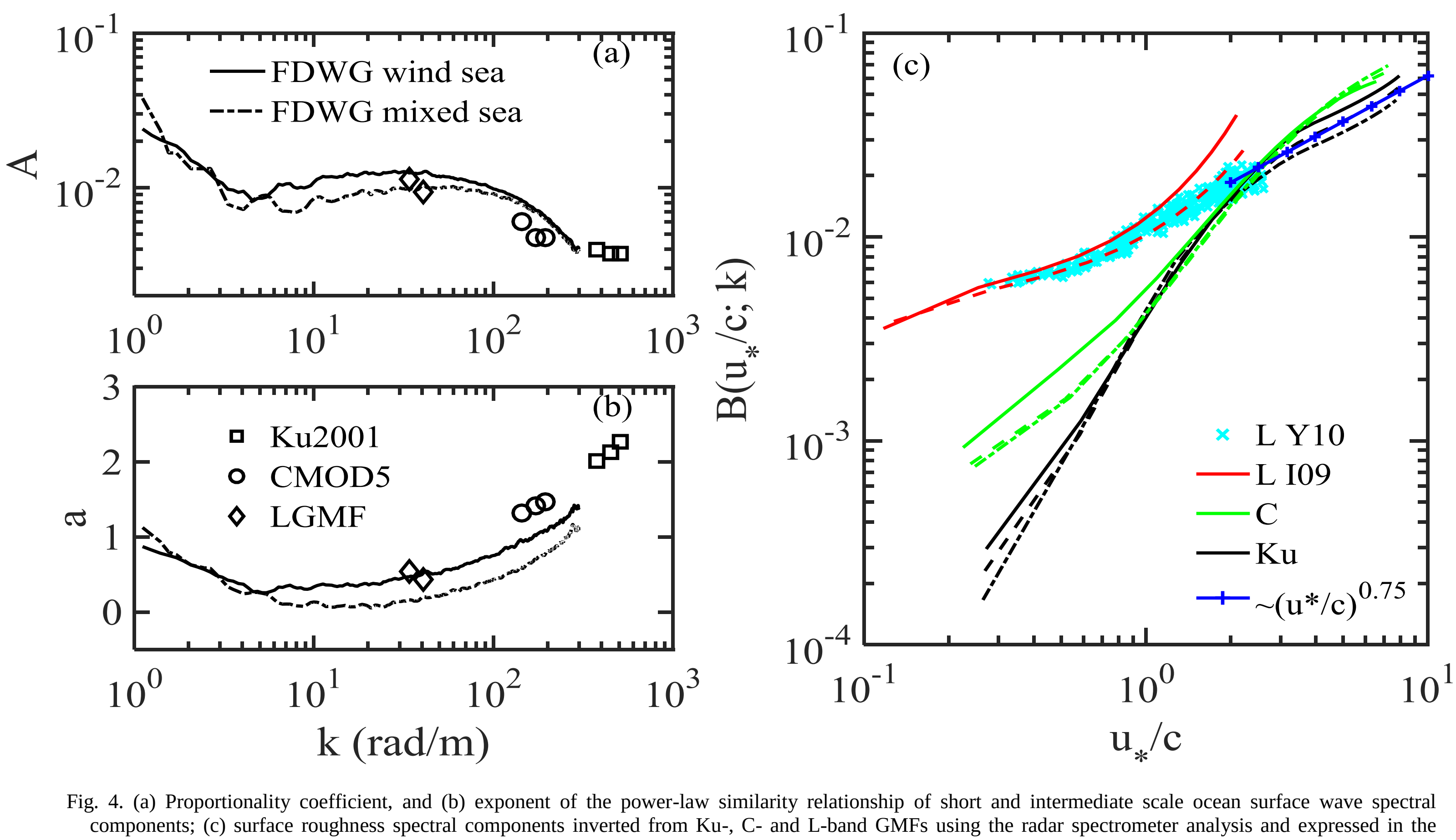

Fig. 4. (a) Proportionality coefficient, and (b) exponent of the power-law similarity relationship of short and intermediate scale ocean surface wave spectral components; (c) surface roughness spectral components inverted from Ku-, C- and L-band GMFs using the radar spectrometer analysis and expressed in the similarity relation function (1). Further description of these data is given in Hwang and Wang (2004a) and Hwang et al. (2013).

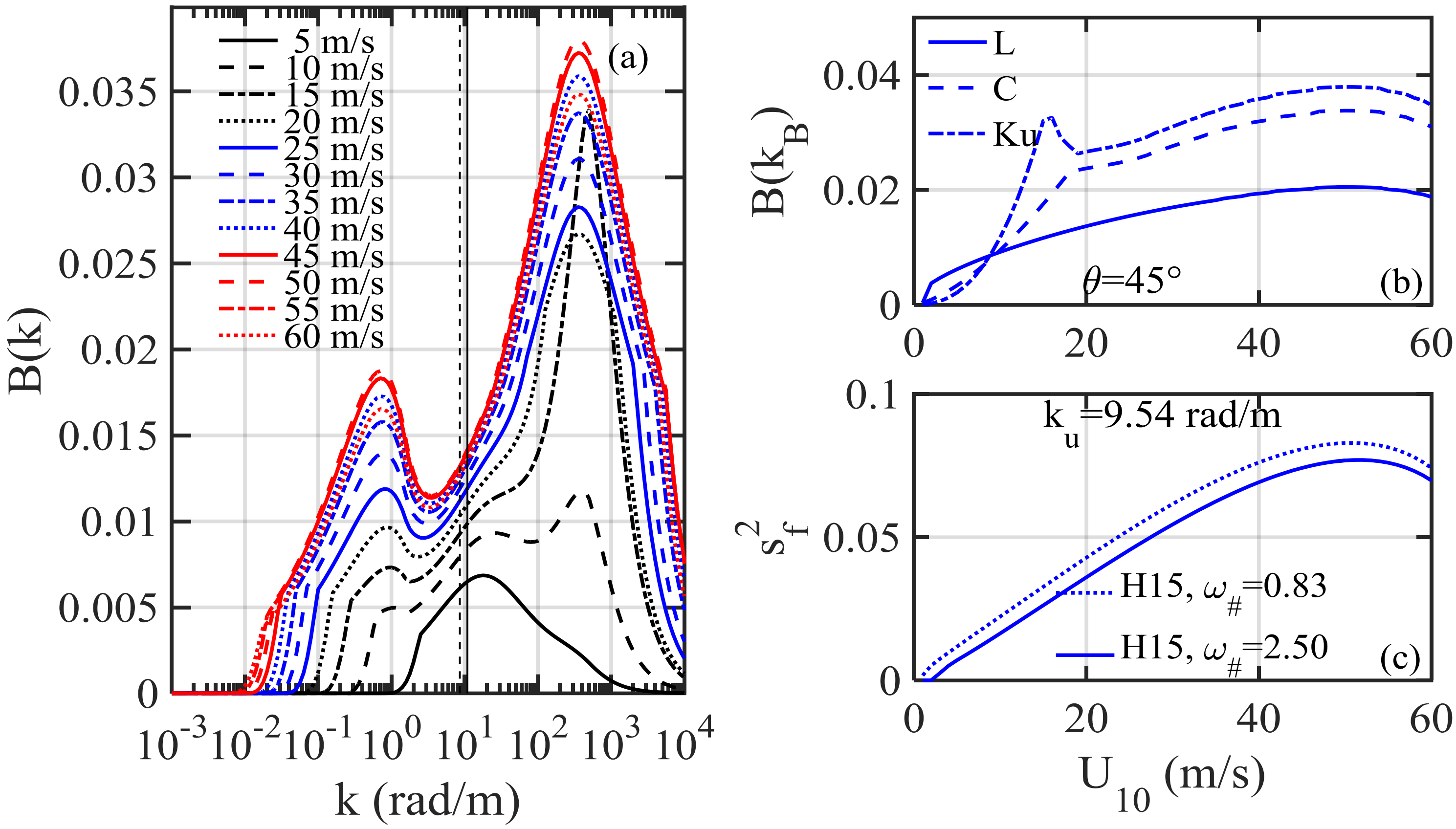

Fig. 5. (a) Dimensionless H spectra at U_{10}=5, 10, … 60 m/s, wave age is 0.4 ($\omega_{\#}$=2.5); (b) examples of the Bragg resonance spectral components at 45° incidence angle for L-, C- and Ku-band frequencies; and (c) low-pass integrated tilting mean square slopes with upper cutoff wavenumber k_u=9.54 rad/m (L band) for mature ($\omega_{\#}$=0.83) and young ($\omega_{\#}$=2.5) seas.

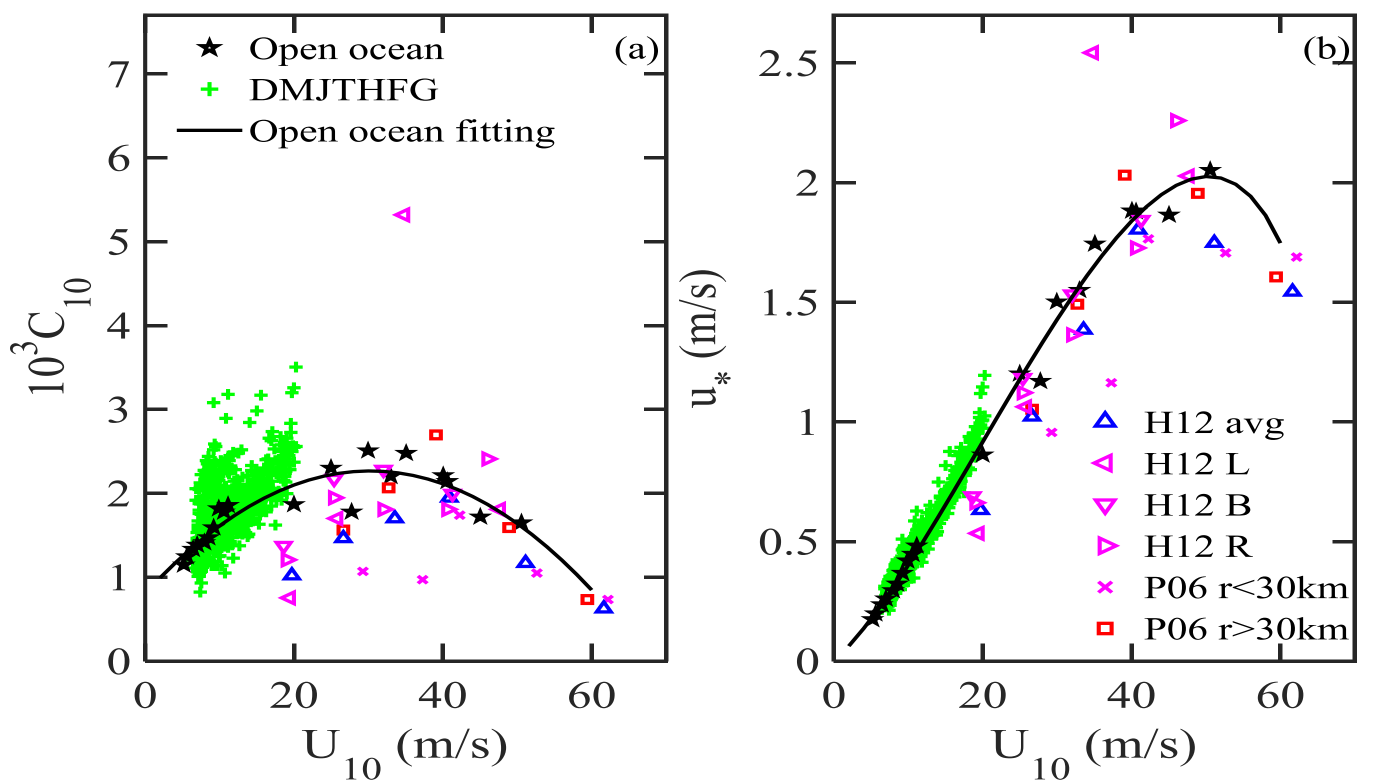

Fig. 6. (a) Ocean surface drag coefficient $C_{10}(U_{10})$, and (b) wind friction velocity $u_*(U_{10})$. Description of field datasets ("Open ocean" and "DMJTHFG") has been given in *Hwang et al.* {2013]. The black line is fitted curve of the open ocean data. Additional measurements in hurricanes (P06: Power (2006), and H12: Holthuijsen et al. (2012)) are shown with different symbols, see text for further description.

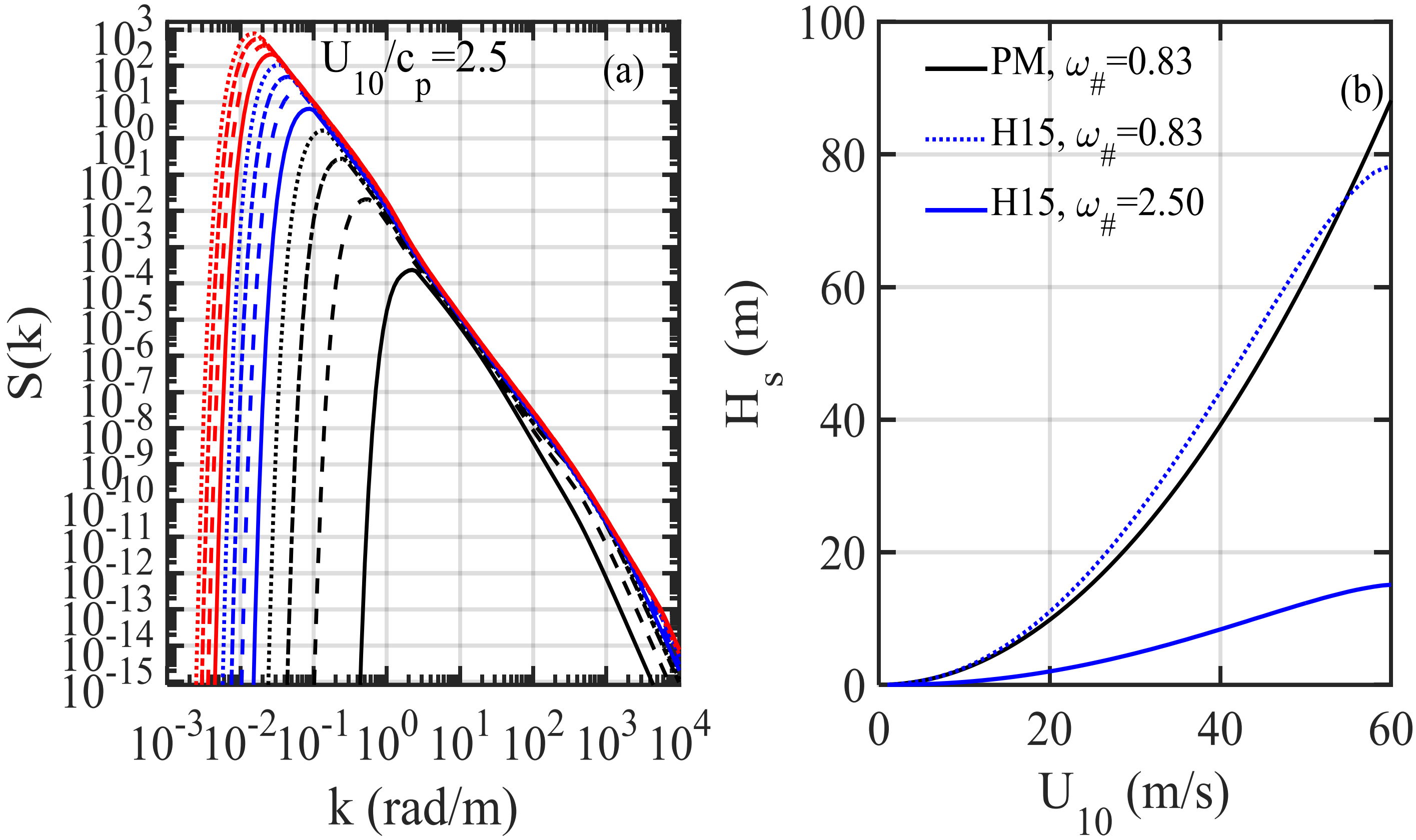

Fig. 7. (a) Displacement H spectra at U_{10}=5, 10, … 60 m/s, wave age is 0.4 ($\omega_{\#}$=2.5) , the line style is the same as that of figure 5a; and (b) the significant wave height based on the H spectra for mature ($\omega_{\#}$=0.83) and young ($\omega_{\#}$=2.5) seas. For comparison of the mature sea condition, the result based on the fully developed PM spectrum (Pierson and Moskowitz)964] is also shown.

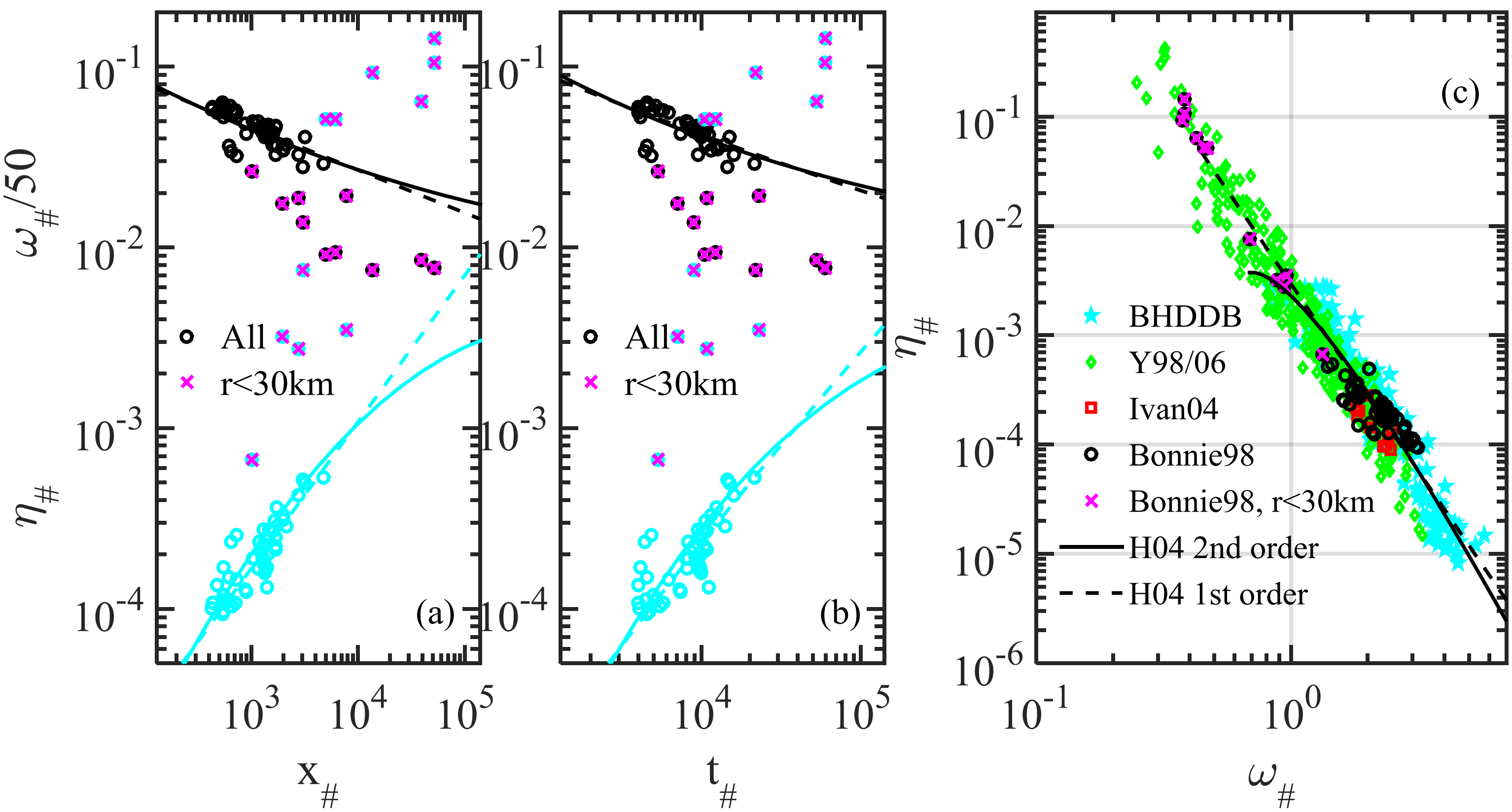

Fig. 8. Fetch- and duration-limited nature of wave development inside hurricanes: (a) $\omega_{\#}(x_{\#})$ and $\eta_{\#}(x_{\#})$, (b) $\omega_{\#}(t_{\#})$ and $\eta_{\#}(t_{\#})$, and (c) $\eta_{\#}(\omega_{\#})$. Data displayed in (a) and (b) are from the 60 SRA spectra collected in Bonnie 1998 (Wright et al. 2001), the ones inside the 30 km circle from the hurricane center (marked with an x) are contaminated by swell. In (c) other hurricane data: SRA measurements from Ivan 2004 (Black et al. 2007) and directional buoy data reported by Young (1998, 2006), and non-hurricane data (BHDDB) are also superimposed. The solid and dashed curves are the 2nd and 1st order fitting curves of the BHDDB data. Further descriptions of these data are given in Hwang and Wang (2004b) and Hwang (2016).

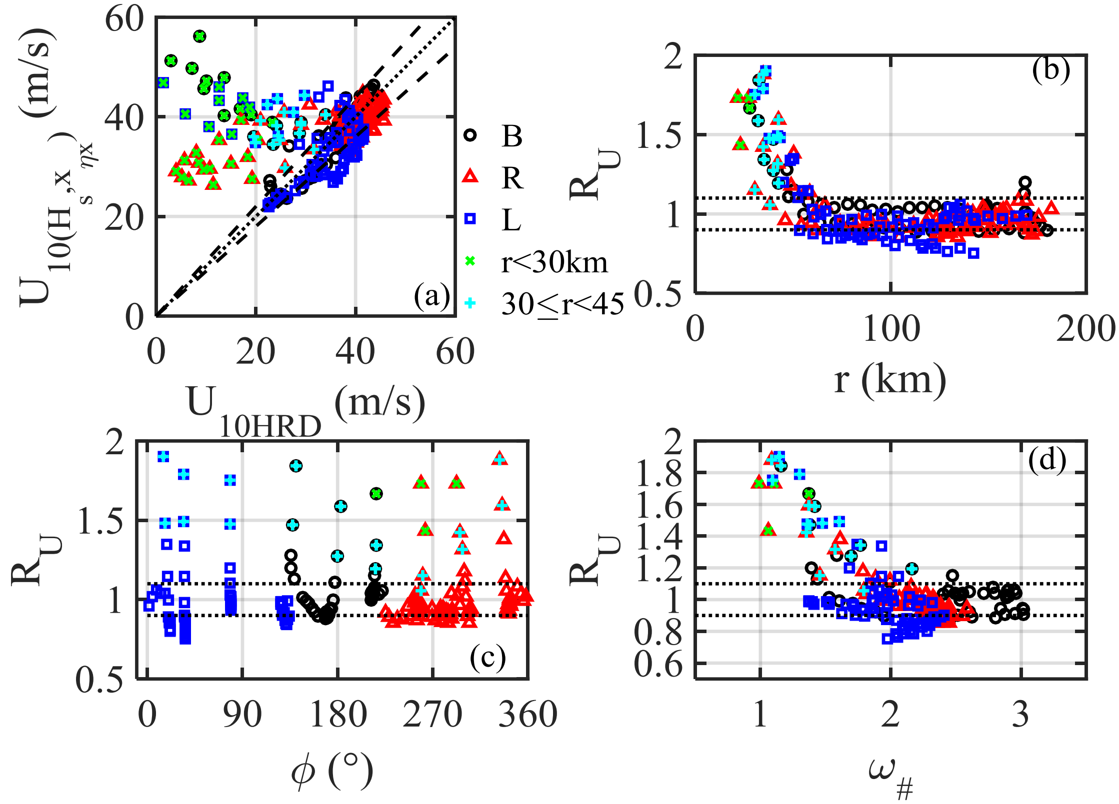

Fig. 9. U_{10} retrieval from H_s using the fetch-limited growth function: (a) Scatter plot of retrieved U_{10} vs. HRD reference; (b) R_U as a function of r; (c) R_U as a function of ϕ; (b) R_U as a function of $\omega_\#$.

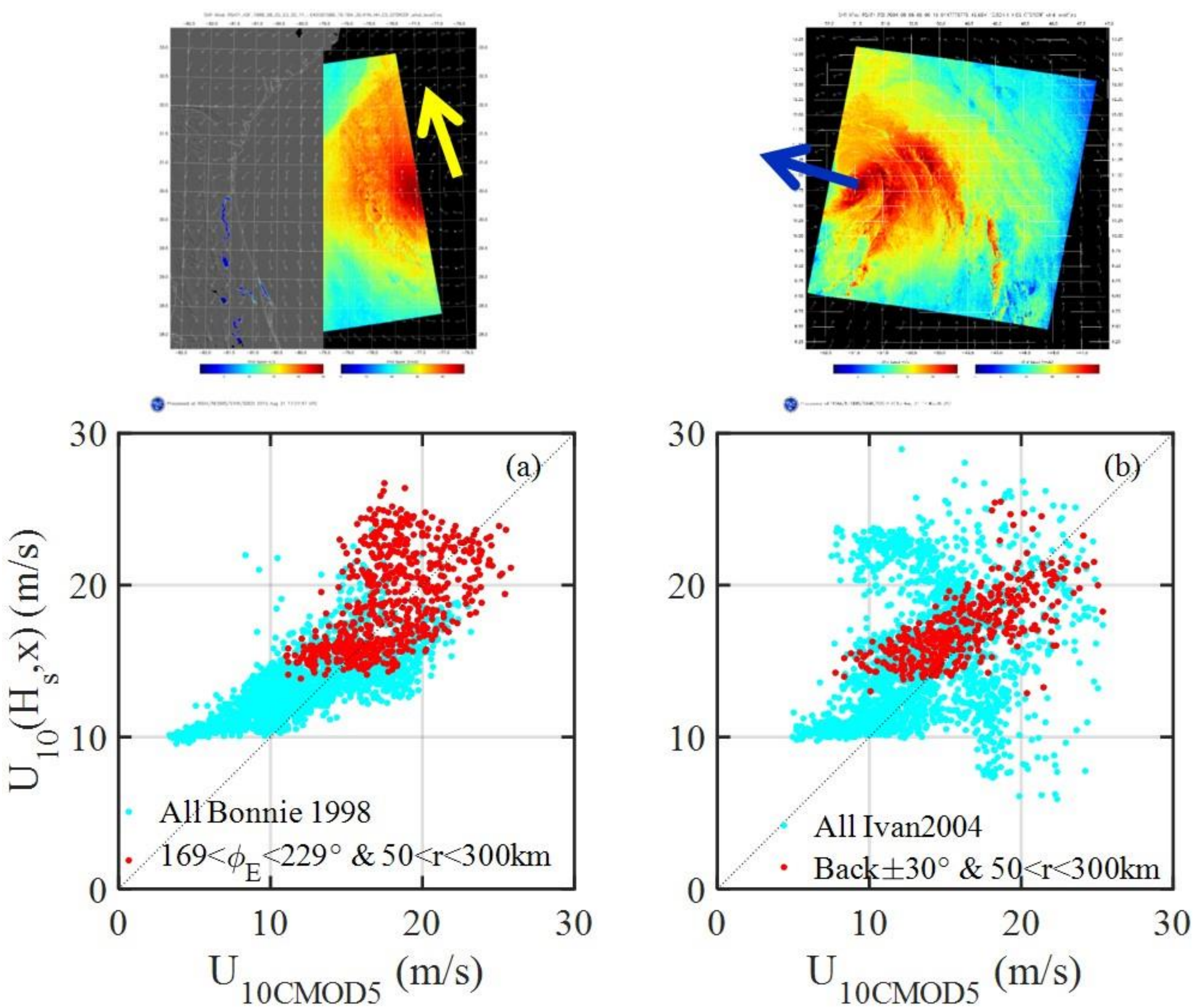

Fig. 10. Comparison of wind speeds retrieved by the fetch-limited growth function and the CMOD5 GMF. (a) Bonnie 1998; (b) Ivan 2004. Shown on top of each panel is the corresponding wind field derived from the RADARSAT image, the superimposed arrow shows the hurricane heading with the root of the arrow at the hurricane center.